Supplementary Information for

All-Solution-Processed Mid-Infrared Electrochromics (ASPIRE) for Thermoregulation with Arbitrary Curvatures

*Pei-Jan Hung[1], Qizhang Li[1], Ting-Hsuan Chen[1,2], Xubing Wu[1], Ching-Tai Fu[1], Yu Han[1], Ronghui Wu[1], Gangbin Yan[1], Qingsong Fan[1], Yunhao Zhao[1], Jiadong Liu[1], Pin-Ruei Huang[1], Yuanke Chen[1], Chenxi Sui[1], Genesis Higueros[1,2], Alex Flores[1], Fengyuan Shi[3], Po-Chun Hsu[1]**

[1]Pritzker School of Molecular Engineering, University of Chicago, Chicago, IL 60637, USA.

[2]Thomas Lord Department of Mechanical Engineering and Materials Science, Duke University, Durham, NC 27708, USA.

[3]Electron Microscopy Core, University of Illinois Chicago, Chicago, IL 60607, USA.

*Corresponding email: pochunhsu@uchicago.edu

Contents Summary

Table S1. Key research advances in electrochromic devices by spectral range (VIS–NIR–MIR)

Working regime	Active material	Mechanism	Solution processability	Substrate	Conformal to 3D curved object?	Ref.
MIR	PEDOT:PSS	Electrochromism	Yes	Glass, PP film, Cu sphere, Cu cup, PLA	Yes	This work
MIR	CNT/Ionic Liquid/CNT	Electrostatic gating	Yes	Glass	No	1
	MWCNT/Ionic Liquid/MWCNT	Electrostatic gating	No	Celgard 2325	No	2
	Ag/Ag^{+}	Electrodeposition	No	ITO/Glass	No	3
	Cu/Cu^{+}	Electrodeposition	No	Copper foil	No	4
	Polyaniline	Electrochromism	No	Au/Microporous PES film	No	5
	Polyaniline	Electrochromism	No	Au/Nanoporous Nylon	Partial	6
	PEDOT:ToS	Electrochromism	No	PE film	No	7
NIR-MIR	WO_3	Electrochromism	No	ITO/Glass	No	8
NIR	ITO Nanocrystals	Surface Plasmon Resonance	Yes	Glass	No	9
	AZO Nanocrystals	Surface Plasmon Resonance	Yes	ITO/Glass	No	10
VIS-NIR	PProDOT($CH_2OC_{18}H_{37}$)2 / PProDOT(CH_2OEtHx)$_2$	Electrochromism	Yes	ITO/Glass	No	11

	WO_3	Electrochromism	No	ITO/Glass	No	12
	Aromatic Polyamides	Electrochromism	Yes	ITO/Glass	No	13
VIS	poly(AcDOT-*co*-EDOT)/Prussian Blue	Electrochromism	Yes	PET Film	No	14
	WO_3	Electrochromism	Yes	Ag grid/PEDOT:PSS /PET Film	Partial	15
	PEDOT:PTS	Electrochromism	Yes	PU	Partial	16
	WO_3	Electrochromism	Yes	PDMS	Partial	17
VIS-NIR-MIR	Polyaniline	Electrochromism	No	Microporous PET/PES film	No	18

Supplementary Note 1 – General concepts of mid-IR electrochromic modulation

To understand the design principles behind mid-IR electrochromic devices, it is essential first to examine the fundamental mechanisms of radiative heat transfer and emissivity. The emission of heat as radiation is a fundamental phenomenon for all objects with a temperature above 0 K. For the human body, which behaves nearly as a black body, heat is primarily radiated in the mid-IR (8-14 μm wavelength) range, peaking at approximately 9.5 μm. In indoor environments, radiation accounts for nearly 50% of the human body's heat dissipation[19]. However, radiative heat transfer is not limited to biological systems. Electronics, industrial equipment, and other heat-generating devices also emit thermal radiation, often operating at temperatures significantly higher than the human body. Managing this heat emission is crucial for ensuring thermal stability, improving energy efficiency, and extending the operational lifespan of these systems. According to Stefan-Boltzmann's law, the power P radiated by an object at temperature T is given by:

$$P = \varepsilon \sigma A T^4 \tag{S1}$$

where ε is the object's emissivity, σ is the Stefan-Boltzmann constant, A is the surface area, and T is the absolute temperature of the object. The emissivity ε, ranging from 1 for an ideal blackbody to 0 for a perfect non-emitter, is the ratio of radiative heat flux emitted by an object to that emitted by an ideal blackbody at the same temperature. This concept is critical for designing systems aimed at dynamic radiative thermoregulation.

For IR-opaque objects with zero transmission, tuning a material's reflectivity (i.e., metallicity) equals tuning its emissivity and, thus, the radiative heat transfer at thermal equilibrium. The tunability of emissivity forms the basis for developing advanced electrochromic materials, such as conjugated polymers, which can modulate radiative heat transfer through precise control of their electronic properties.

Supplementary Note 2 - The tuning mechanism of mid-IR electrochromism

The strategies for modulating light-matter interactions in electrochromic conjugated polymers vary among targeted spectra. In the visible regime, modulation primarily focuses on tuning the HOMO-LUMO gap (i.e., the band gap E_g) of π-conjugated polymers. The maximum absorption peak of π-conjugated polymers can be finely tuned through synthetic approaches, such as controlling conjugation length, adding functional substituents, or modifying polymer sterics. These adjustments enable π-conjugated polymers to exhibit a full palette of colors in the visible spectrum, extending even into the ultraviolet (UV) and near-infrared (NIR) ranges[20,21].

In the mid-infrared (MIR) and far-infrared (FIR) regions, the light-matter interactions of conjugated polymers are primarily governed by their free-carrier responses. Optical modulation therefore relies on tuning the polymers' free carrier density n_c (and hence their conductivity), which in turn alters the plasma frequency ω_p. In the conducting state, metallic conjugated polymers typically exhibit carrier densities on the order of $10^{21}\ cm^{-3}$, corresponding to a plasma frequency in the infrared regime ($\hbar\omega_p \approx 1\ eV$)[22-24]. The complex permittivity, $\tilde{\varepsilon}(\omega) = \varepsilon' + i\varepsilon''$, can be described by the Drude model as

$$\tilde{\varepsilon}(\omega) = 1 - \frac{\omega_p^2}{\omega^2 + i\gamma\omega} \tag{S2}$$

where ω is the angular frequency of the incident electromagnetic (EM) wave, i is the imaginary unit, and γ is the momentum scattering rate. The plasma frequency ω_p is given by

$$\omega_p = \sqrt{\frac{n_c e^2}{\varepsilon_0 m_0}} \tag{S3}$$

where n_c is the charge carrier density, e is the elementary charge, ε_0 is the permittivity of free space, and m_0 is the effective mass of the charge carrier. Thus, by controlling the free carrier density of conjugated polymer, one can effectively tune their plasma frequency and thereby modulate infrared reflectivity.

To further illustrate the relationship between the conducting polymer's carrier density and its reflectivity, we consider a representative scenario where the EM wave is normally incident on a bulk polymer (Fig. S2a), with a thickness much greater than the corresponding skin depth. Under this condition, the film behaves as an optically thick medium, and its reflectivity can be written as

$$R = \left|\frac{\tilde{n}-1}{\tilde{n}+1}\right|^2, (film\ thickness \gg skin\ depth) \quad \text{(S4)}$$

where $\tilde{n} = \sqrt{\tilde{\varepsilon}}$ is the complex refractive index. Incorporating equations (S2)-(S4), the reflectivity as a function of carrier density can be calculated at 10 μm, corresponding to the peak wavelength of human body radiation. It is assumed there are no infrared-activated vibrations (IRAVs), and the momentum scattering rate γ is set to $^{0.1}\,\omega_p$, where ω_p is the plasma frequency. As shown in Fig. S2b, the reflectivity increases with carrier density, which can be achieved by electrochemically oxidizing the polymer and introducing polarons and bipolarons. Conversely, when the polymer is electrochemically reduced and these carriers are removed, the charge carrier density decreases, leading to lower reflectivity and insulating behavior. Notably, the reflectivity varies significantly as the frequency of the incident EM wave approaches the polymer's plasma frequency due to plasmon resonance between the incident wave and the conjugated polymer.

Additionally, the increase in charge carrier density enhances the conjugated polymer's optical metallicity, as shown in Fig. S2c. The simulation depicts that as the charge carrier densities increase from $n_{c,1}$ to $n_{c,3}$, the plasma frequency rises, and the real part of the relative permittivity becomes more negative. For incident EM waves with a frequency of $\omega < \omega_p$, the real part of the permittivity of the conjugated polymer is negative, leading to an imaginary refractive index, meaning that its extinction coefficient κ is large. As a result, the conjugated polymer exhibits high attenuation[25]. The incoming evanescent waves decay exponentially within the material's skin depth. When the thickness of the bulk material is much greater than its skin depth, the evanescent fields penetrate only a short distance, resulting in minimal absorption within the medium, and the majority of the waves are reflected into the air ($R \approx 1$), similar to what is observed in metals. The more negative relative permittivity, the more "metal-like" the conjugated polymer becomes.

Ideally, identifying a conjugated polymer with high intrinsic conductivity is critical. If the polymer has low mobility or insufficient doping efficiency (low conductivity), the

electrochemically induced carrier density n_c will remain moderate. In this regime, the plasma frequency ω_p may fall within or below the mid-IR target frequency. Consequently, the material does not transition into a metallic reflector but instead enters a "lossy dielectric" state characterized by strong free-carrier absorption (high extinction coefficient κ, but low real permittivity magnitude). According to Kirchhoff's law, this high absorption results in high emissivity, preventing the device from achieving the desired low-emissivity (reflective) state. This phenomenon is experimentally demonstrated in Fig. S1b, where the low conductivity commercial PANI ($\sigma \approx 5.5 \pm 1.0\ S/cm$) exhibit persistently high emissivity upon oxidation, in stark contrast to the highly conductive house-synthesized PANI ($\sigma \approx 244.3 \pm 4.9\ S/cm$) in Fig. S1a. The detailed electrical conductivity measurements and comparisons are summarized in Table S6. This confirms that insufficient conductivity leads to a lossy dielectric state rather than a metallic reflective state, thereby limiting the emissivity tunability.

Experimental Verification of Optical Thickness

To validate the assumption that $1\ \mu m$ thick PEDOT:PSS layer behaves as a bulk material (i.e., is optically thick), we performed spectroscopic ellipsometry to determine the skin depth. The skin depth (δ), defined as the distance over which the electric field amplitude decays by a factor of $1/e$, is derived from the measured absorption coefficient (α) according to the relation $\delta = {}^{2}/_{\alpha}$.

As shown in Fig. S2d-e, the pristine PEDOT:PSS film exhibits a skin depth of approximately $\delta \approx 200\ nm$ at $10\ \mu m$. The transmittance (T) of light traveling through a film of thickness z follows the Beer-Lambert law:

$$T = \frac{I}{I_0} = e^{-2z/\delta}$$

The relationship between film thickness (in multiples of δ) and the remaining transmittance is summarized in the Table S2 below.

Table S2. Theoretical transmittance decay as a function of film thickness (in multiples of skin depth δ)

Thickness (z)	Theoretical Transmittance ($T = e^{-2z/\delta}$)	Experimental Context
δ	13.5%	
$\approx 1.8\delta$	2.7%	Reflectance saturation observed (Fig. S2f)
3δ	0.25%	
4δ	0.03%	
5δ	$< 0.01\%$	ASPIRE Device (thickness $\geq 1\mu m$)

As demonstrated in Fig. S2f, the reflectance spectra for films with thickness $\approx 359\ nm$ ($\approx 1.8\delta$) already show saturation. This is consistent with the theoretical prediction that the light intensity reaching the bottom interface is negligible ($\approx 2.7\%$), confirming that the substrate signal is effectively masked. The ASPIRE device, with a thickness exceeding $1\ \mu m$ ($> 5\delta$), provides an even higher safety margin to ensure the film is optically thick.

In conclusion, this Note establishes a comprehensive physical framework, combining the simplified Drude model with experimental validation, to explain the active emissivity modulation in our devices. Beyond explaining our specific results, this framework elucidates the universal physical logic that bridges carrier density (n_c), plasma frequency (ω_p), and infrared reflectivity in metallic conjugated polymers. Crucially, by quantitatively defining the skin depth ($\delta \approx 200\ nm$) of PEDOT:PSS as a fundamental design parameter, this Note provides a clear benchmark for achieving the "optically thick" state necessary for effective thermoregulation. The observed reflectance saturation at $\approx 1.8\delta$ (Fig. S2f) validates this theoretical boundary, serving as a practical guide for researchers to optimize active layer thickness and conductivity in the design of advanced radiative materials.

Supplementary Note 3 - Influence of ionic conductors on PEDOT:PSS electrochromic performance

At the device level, ionic conductors play a central role in enabling electrochemical modulation of conjugated polymers, such as PEDOT:PSS. Although mid-IR emissivity changes originate from variations in carrier density within the polymer backbone, the type and mobility of ions in the electrolyte strongly influence how efficiently this carrier modulation occurs.

Previous studies have shown that the valence state, ionic radius, and mobility of ions affect switching kinetics, coloration efficiency, and cycling stability in PEDOT:PSS-based devices. For example, Gu et al. reported that higher-valence ions lead to greater coloration efficiency and faster switching, while smaller-radius ions such as Li^+ or Al^{3+} cause less structural disruption and enable longer cycle lifetimes[26]. Importantly, simple ions such as Li^+ and Cl^- lack intrinsic mid-IR absorption modes and therefore do not contribute directly to spectral changes. Operando NMR studies by Lyu et al. further demonstrated that cations (e.g., Na^+ in their work) serve as the primary mobile species during the electrochemical oxidation and reduction[27], highlighting their roles in charge compensation.

Taken together, these findings indicate that while ions do not directly alter the mid-IR optical responses, their transport properties govern the degree and reversibility of carrier-density modulation in PEDOT:PSS. Thus, careful selection of ionic conductors is crucial. Table S3 compares these parameters.

Although multivalent ions such as Mg^{2+} and Al^{3+} have been shown to reversibly operate in PEDOT:PSS-based electrochromic systems, they are not adopted in the present work primarily due to their limited aqueous solubility, which precludes access to the high-concentration "water-in-salt" regime required to achieve a wide electrochemical window. Similarly, K^+ and Na^+ lack sufficient solubility (below ~10 m) to support the targeted operating regime. In contrast, Li^+ provides an optimal global balance: it possesses the unique high solubility (~ 19.9 m) suitable for the "water-in-salt" electrolyte (see Supplementary Note 4), while maintaining a monovalent charge and small ionic radius (0.76 Å), enabling efficient and reversible electrochemically induced carrier-density modulation in PEDOT:PSS.

To experimentally validate this size effect, we performed a control experiment comparing small (Li^+) and bulky (TBA^+) cations in an acetonitrile environment to isolate the steric

contributions. As shown in Fig. S17, the bulky TBA^+ ions exhibit a significantly compressed CV responses compared to Li^+, confirming that steric hindrance from larger ionic radii severely limits doping efficiency and charge storage capacity.

Table S3. Comparison of physical properties of common cations and anions

Ion	**Valence (z)**	**Effective Ionic Radius † (Å)**	**Hydrated Radius [c] (Å)**	**Ionic Mobility ‡ ($10^{-8} m^2 V^{-1} s^{-1}$)**	**Solubility in water ($mol/kg\ H_2O$, ~25 ℃)**	**Suitability for ASPIRE**
Li^+	+1	0.76	3.82	4.01	~ 19.9 m	**High** (Optimal balance)
Na^+	+1	1.02	3.58	5.19	~ 6.2 m	Low (insufficient solubility)
K^+	+1	1.38	3.31	7.62	~ 4.8 m	Low (insufficient solubility)
Mg^{2+}	+2	0.72	4.28	5.49	~ 5.9 m	Low (Insufficient solubility)
Al^{3+}	+3	0.54	4.75	6.32	~ 3.4 m	Low (Insufficient solubility)
Cl^-	-1	1.81	3.32	7.91	-	**High** (Stable counterion)

Note:
† Effective ionic radii for inorganic ions are based on Shannon's data for coordination number (CN) = 6. [a]
‡ Ionic mobility (u) is calculated from limiting molar conductivities (λ^0) and valence (z) using $u = \lambda^0/(|z|F)$ with data sourced from the CRC Handbook. [b] F is the Faraday constant.

References for Table S3:
[a] Shannon, R. D. Acta Crystallographica Section A 32, 751-767 (1976).
[b] Rumble, J. R. CRC Handbook of Chemistry and Physics. 106th Edition (CRC Press, 2025).
[c] Nightingale Jr, E. R. Journal of Physical Chemistry 63, 1381-1387 (1959).

Supplementary Note 4 – Expanding the electrochemical stability window with a "Water-in-salt" hydrogel strategy

Mid-IR emissivity tunability in PEDOT:PSS is directly governed by its charge carrier density (Supplementary Note 2). To achieve a wide tuning range, the material must be switched between a highly oxidized state (high carrier density, low emissivity) and a deeply reduced state (low carrier density, high emissivity). However, as predicted by the Drude model and the Fresnel equation, the reflectivity of PEDOT:PSS is a strong function of its charge carrier density (Fig. S2b). Our simulations show that the reflectivity plateaus at a value of approximately 0.8 as carrier density increases. This finding is consistent with a previous report that the DC conductivity of PEDOT:PSS, which is proportional to carrier density, plateaus at around 1000 S/cm[28]. That indicates that further increasing the conductivity in the oxidized state has little effect on emissivity, and that mid-IR tunability instead depends critically on achieving a deeply reduced state. Within a limited ±1V potential window (Fig S6), PEDOT:PSS modulation yields only ~ 7.6%, while a ±2 V potential window can result in a greater modulation of 19.5% (Fig 3a).

Accordingly, the electrolyte must combine a broad electrochemical stability window, high ionic conductivity, solution processability, and strong adhesion to 3D curved substrates. To meet these requirements, we employed a PAM/LiCl hydrogel, which adheres well to curved surfaces while leveraging a "water-in-salt" strategy to broaden its potential window. As shown in the linear sweep voltammetry (LSV) scan in Fig. S7, the hydrogel electrolyte exhibits a remarkably wide electrochemical stability window of 4.67 V, with the onset of the cathodic current at approximately -2.67 V and the anodic current at +2.0 V.

This performance stands in contrast to bulk aqueous electrolytes. It is achieved because highly concentrated salt electrolytes (>10 m) reduce water activity, as most water molecules are coordinated within the Li^+ solvation shell[29]. Increasing the salt concentration effectively expands the electrochemical stability window[30]. In addition, the 3D crosslinked polymer networks of PAM bind water molecules and suppress their mobility, thereby slowing down the decomposition kinetics of water[31]. Previous molecular dynamics simulations also support the existence of strong interactions between water molecules and the polymer matrix[32,33], which contribute to the enhanced electrochemical stability observed in "water-in-salt" hydrogel electrolyte systems[31,34].

Hydrogel Electrolyte Characterization

The lithium ion concentration within the PAM hydrogel was precisely determined using Inductively Coupled Plasma Mass Spectrometry (ICP-MS), with details of the procedure provided in the Methods section.

To calculate the concentration (moles per liter of water), we first quantified the water content of the hydrogel. This was achieved by measuring the mass change after a lyophilization process. A total of four hydrogel samples were frozen at -80°C for 24 hours and subsequently vacuum-dried for 72 hours. As shown in Table S4, this process yielded an average water content of 51.95 ± 0.1 % by mass.

Using this average water content, we calculated the total weight of water in the ICP-MS samples. The ICP-MS analysis revealed a lithium concentration of 10.72 M, based on a measurement of 1104.5 ± 3.02 μmol of Li in a sample containing 0.103 g of water.

Table S4. Hydrogel water content calculation

PAM/LiCl hydrogel	(1) PAM/LiCl hydrogel weight before freeze-drying (g)	(2) PAM/LiCl hydrogel weight after freeze-drying (g)	(3) $-\Delta m_{loss} = m_{w}$ (g)	(4) water content % $m\% = \frac{(3)}{(1)}$	(5) average water content % in PAM/LiCl hydrogel
Sample 1	2.2191	1.0661	1.153	51.96%	51.95±0.1%
Sample 2	2.2015	1.0615	1.14	51.78%	
Sample 3	2.2046	1.0572	1.1474	52.04%	
Sample 4	2.2056	1.0587	1.469	52.00%	

Supplementary Note 5 – Calculation of ASPIRE device thermal regulation capability

Radiation heat transfer

We consider a device at temperature T_{dev} surrounded by an environment at temperature T_{amb}, treated as a blackbody, ($\varepsilon = 1$). The net radiative heat flux Q_{rad} from the device to its environment is given by:

$$Q_{rad} = \int_0^{2\pi}\int_0^{\pi/2}\int_0^{\infty} \varepsilon(\lambda)\left[I_{BB}(\lambda,T_{amb}) - I_{BB}(\lambda,T_{dev})\right]\sin\theta\cos\theta d\lambda d\theta d\varphi \quad \text{(S5)}$$

where $\varepsilon(\lambda)$ is the wavelength-dependent device emissivity, λ is the wavelength, θ is the polar emission angle, φ is the azimuthal emission angle, and $I_{BB}(\lambda,T_{amb}) = \frac{2hc^2}{\lambda^5}\frac{1}{e^{hc/(\lambda k_B T)} - 1}$ is the spectral radiance of a blackbody at temperature T with h the Planck constant, k_B the Boltzmann constant, and c the light speed in vacuum. The integration wavelength range (2.5 μm to 20 μm) covers the dominant thermal radiation near 300 K.

Heat Balance

At thermal equilibrium, the total heat balance is given by:

$$Q = Q_{rad} + Q_{cod} + Q_{cov} \quad \text{(S6)}$$

Where Q is the constant heat generation of the device, Q_{cod} is the conductive heat flux, and Q_{cov} is the convective heat flux. Conduction and convection are combined as:

$$Q_{cod} + Q_{cov} = h(T_{dev} - T_{amb}) \quad \text{(S7)}$$

where h is the effective heat transfer coefficient ($\frac{W^2}{m^2 K}$). Combining Eqs. (S5) - (S7), the equilibrium device temperature T_{dev} can be derived for different ambient conditions. In the radiation-only limit ($h = 0$), the equilibrium device temperature is defined as T_{dev}^{max}.

Operating window and ambient tolerance expansion

As described in the main text, the operating window is defined as $T_{dev}^{max} - 1\ ℃$ to $T_{dev}^{max} - 5\ ℃$, representing the acceptable internal device temperature range for stable operation. The dark blue spans (ΔT_1 and ΔT_2 in Fig.3d) represent the ambient temperature ranges over which the device remains within this operating window. The operating temperature expansion is defined as $\Delta T_1 - \Delta T_2$.

Supplementary Note 6 – The convection coefficient *h* and real-life scenarios

To evaluate the capability of the ASPIRE device under various convection environments, we correlated the convection coefficient h with real-life scenarios with established models. For an indoor scenario with air speeds $0.2 \leq v < 0.8$ m/s, the regression model proposed by de Dear et al.[35] was employed:

$$h_c = 10.3v^{0.6} \left(\frac{W}{m^2K}\right) \quad (6)$$

where h_c is the convection coefficient, and v is the wind speed (m/s). Using this model, we connected real-life scenarios with corresponding wind speeds and convection coefficients, as summarized in the table below:

Table S5. Examples of convection coefficients at different wind speeds

Wind speed v (m/s)	Convective coefficient h $\left(\frac{W}{m^2K}\right)$	Real life scenario
0.1 – 0.2	2.5 – 4	Free convection in a closed room
0.2 – 0.5	4 – 7	Mild natural convection (e.g., breeze from an A/C vent)
0.5 – 0.8	7 – 9	Natural forced convection (e.g., open window breeze)
> 0.8	> 9	Strong forced convection (e.g., industrial fan or brisk wind outdoor)

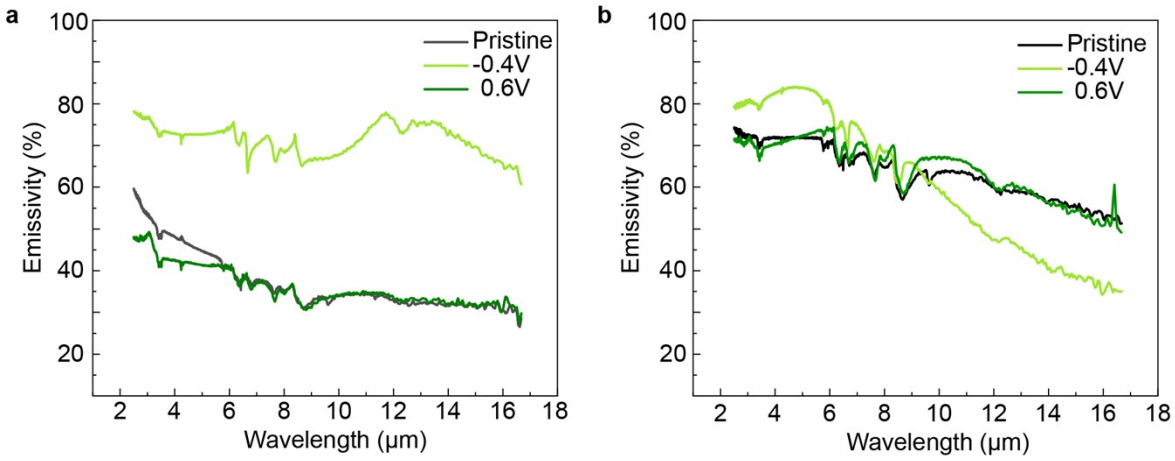

Fig. S1. Influence of polymer conductivity on mid-IR emissivity tunability.
(a) Emissivity spectra of house-synthesized high-conductivity polyaniline (PANI, emeraldine salt state), prepared via solid-liquid interfacial polymerization (SLIP-e), showing pronounced modulation ($\Delta\varepsilon \approx 0.4$) between –0.4 V and 0.6 V (vs. Ag/AgCl). Four-point probe measurements indicate a high DC electrical conductivity of $\sigma \approx 244.3 \pm 4.9\ S/cm$. **(b)** Commercial low-molecular-weight PANI (20 kDa, emeraldine salt state; Sigma-Aldrich, #556378, doped with camphor sulfonic acid) maintains high emissivity under both oxidation and reduction, resulting in minimal tunability. This sample exhibits a significantly lower DC conductivity of $\sigma \approx 5.5 \pm 1.0\ S/cm$, confirming that insufficient conductivity leads to a lossy dielectric state rather than a metallic reflective state. Both materials were dissolved in 1.5% m-cresol and drop-cast onto a CNT/glass substrate. Electrochemical switching was performed in a standard three-electrode setup (0.5 M HCl electrolyte, Ag/AgCl reference, Pt counter electrode).

Table S6. DC electrical conductivity comparison between house-synthesized and commercial PANI

Sample	Entry	Sheet Resistance $R_s(\Omega/sq)$	film thickness t (cm)	DC Conductivity (S/cm) $\sigma = \frac{1}{R_s \cdot t}$
In-house synthesized PANI:CSA in 1.5% m-cresol	1	8.138	0.000499	246.25
	2	7.806	0.000517	247.98
	3	8.565	0.000489	238.71
			average (Mean ± S.D)	244.3 ± 4.9
Sigma-Aldrich MW 20K PANI in 1.5% m-cresol (#556378)	1	506.86	0.000364	5.42
	2	964.86	0.000244	4.24
	3	434.68	0.000405	5.67
	4	314.68	0.000476	6.67
			average (Mean ± S.D)	5.5 ± 1.0

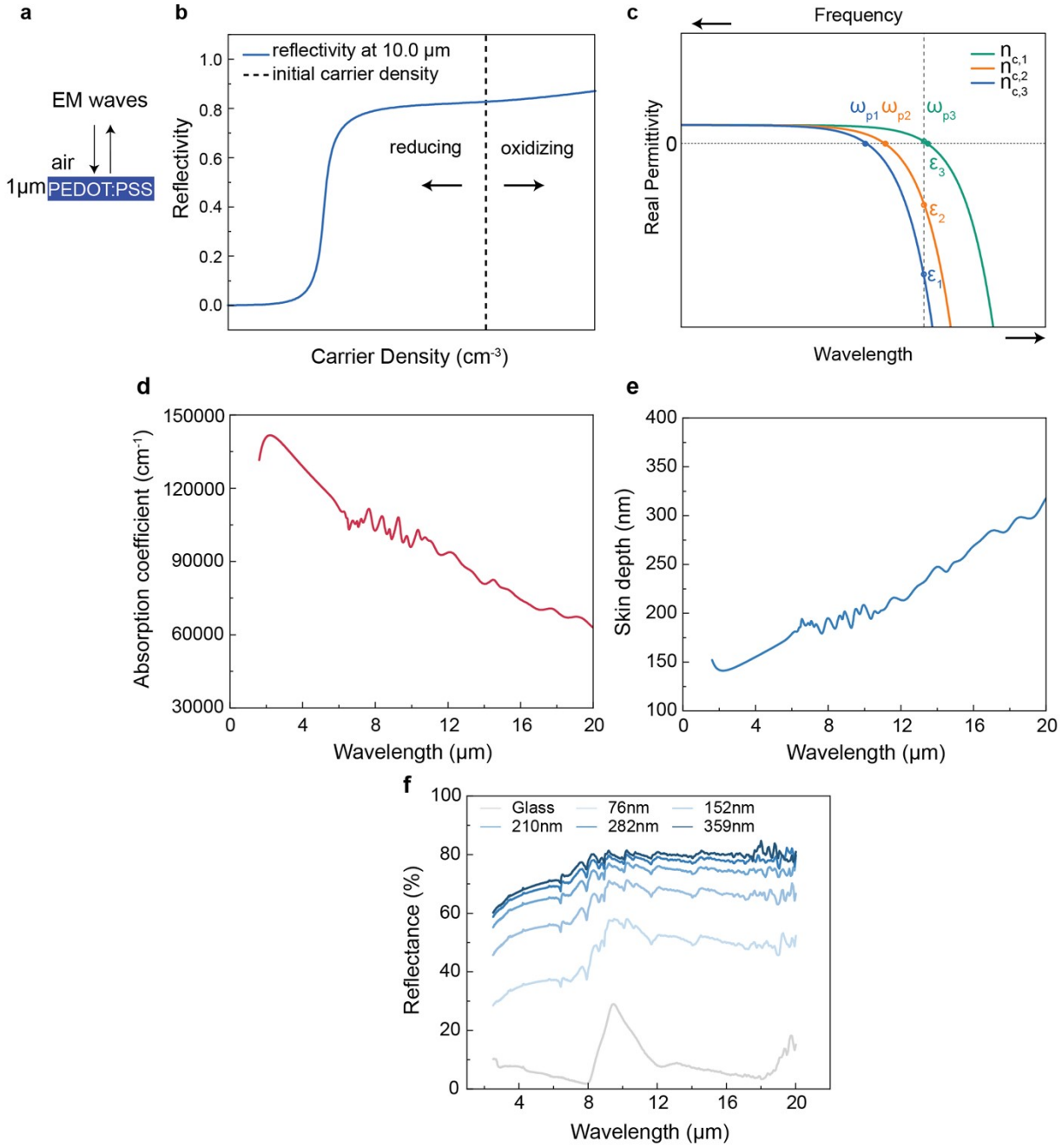

Fig. S2. Simulation and experimental verification of metallic conjugated polymer light-matter interaction modulation.

(A-C) Theoretical simulation using a simplified Drude Model: **(A)** Schematic of the simulation model: PEDOT:PSS is treated as a bulk material with single-interface reflectivity, assuming its thickness is much greater than its skin depth. **(B)** Simulated reflectivity modulation as a function of charge carrier density at a fixed wavelength of 10 μm. **(C)** Simulated evolution of the real part of relative permittivity and plasma frequency with increasing charge carrier density ($n_{c,1} < n_{c,2} < n_{c,3}$). As the carrier density rises, the plasma frequency increases ($\omega_{p1} > \omega_{p2} > \omega_{p3}$),

shifting the zero-crossing point to shorter wavelengths (leftwards), and the real part of the permittivity becomes more negative ($\varepsilon_1 < \varepsilon_2 < \varepsilon_3$), indicating an increase in the metallicity of PEDOT:PSS.
(D-F) Experimental verification of the "optically thick" assumption: **(D)** Absorption coefficient (α) of pristine PEDOT:PSS film in the mid-IR range, measured by spectroscopic ellipsometry. **(E)** Calculated skin depth ($\delta = {}^{2}/_{\alpha}$) as a function of wavelength, showing a skin depth of approximately 200 nm at 10 µm. **(F)** Thickness-dependent reflectance spectra of PEDOT:PSS films on glass substrates. The reflectance increases with thickness and saturates when the film thickness exceeds $\approx 359\,nm$ (1.8δ), confirming that the substrate signal is fully masked. This validates that the 1 µm thick active layer in the simulation behaves as an optically thick bulk material, justifying the use of the single-interface Fresnel model in (a).

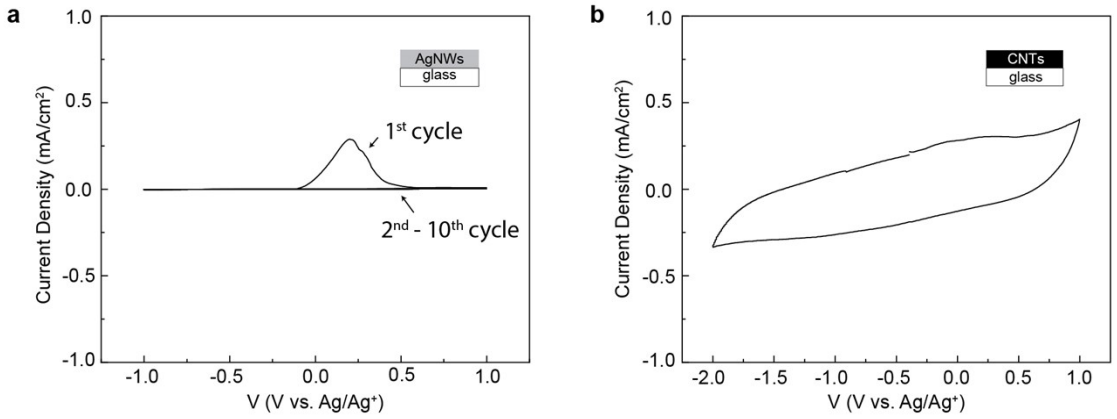

Fig. S3. Cyclic voltammetry for (a) silver nanowires (AgNWs) and (b) carbon nanotubes spray-coated on a glass substrate as a current collector. The experiment was carried out in a three-electrode configuration with carbon paper as the counter electrode, a $Ag/AgNO_3$ organic reference electrode, and a 0.1M $LiClO_4$/acetonitrile electrolyte at room temperature. The reference electrode was calibrated using 0.01 M ferrocene/ferrocenium in the same electrolyte and $E^{Fc/Fc^+}_{1/2} = 0.106\,V$ vs. Ag/Ag^+. The scan rate was 20 mV/s. The upper right inset shows the configuration of both samples. A pronounced oxidation peak for silver ($Ag \rightarrow Ag^+ + e^-, 0.8\,V\ vs.\ SHE$) can be observed in the first cycle, and the subsequent current nearly drops to zero, indicating the corrosion of AgNWs networks. On the other hand, CNTs exhibit a stable and larger potential window without redox peaks, which is suitable for heterogeneous mixed conductors.

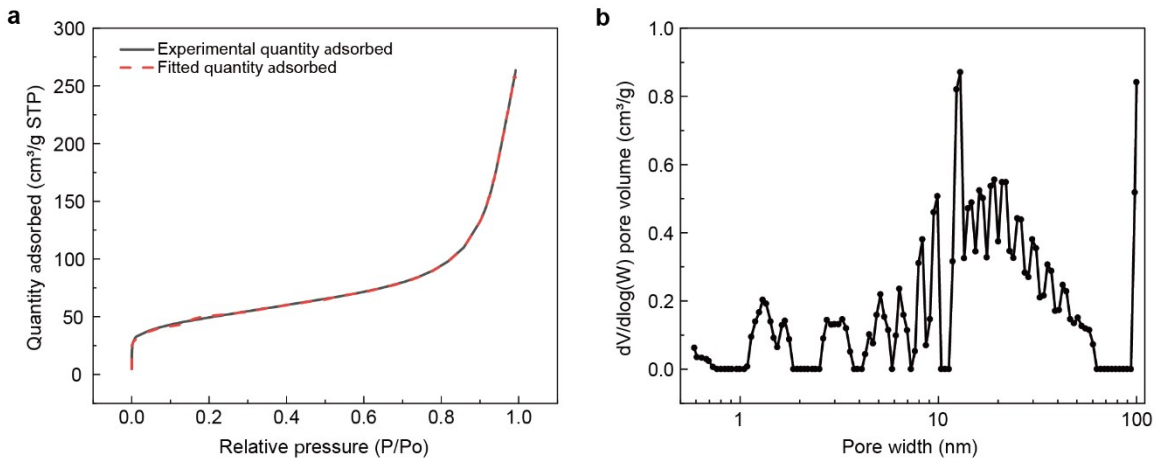

Fig. S4. N_2 adsorption analysis of CNT powders. (A) Pore volume distribution was analyzed by the non-local density functional theory (NLDFT) model. (B) Experimental data of the absorption isotherm and the fitting curve. The data show that the pore sizes of the CNTs are mainly in the range of 10-50 nanometers.

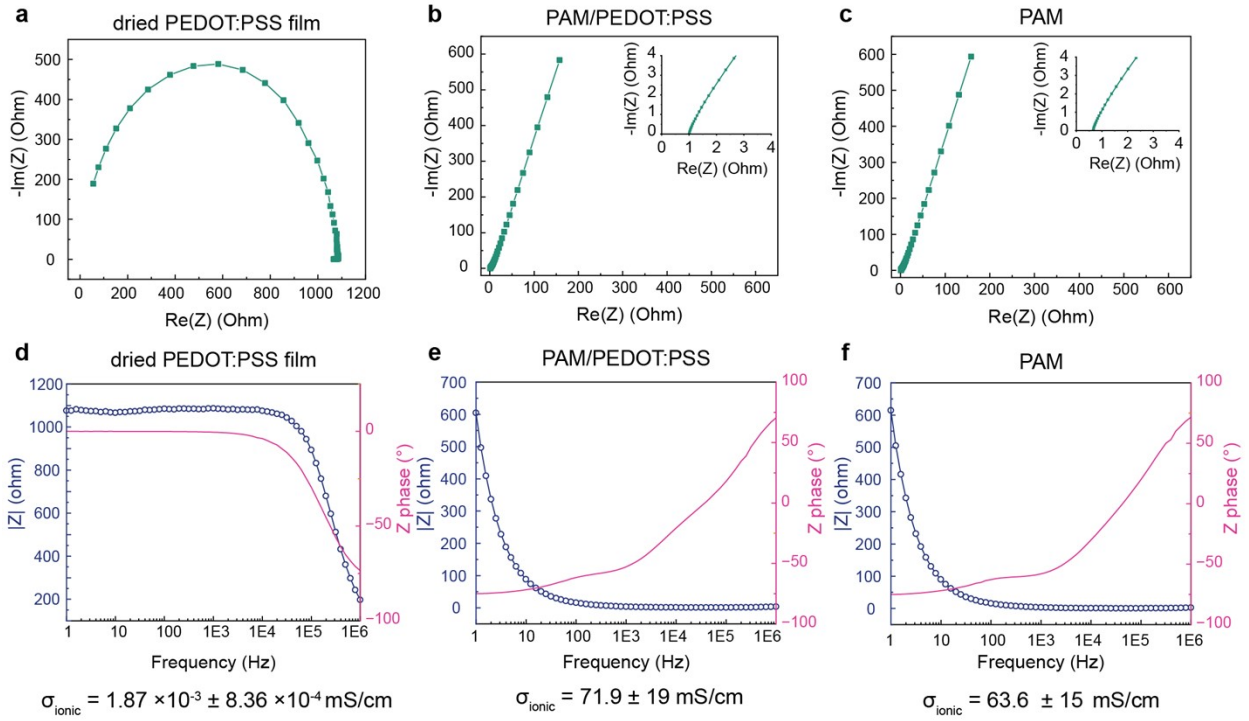

Fig. S5. Electrochemical impedance spectroscopy (EIS) analysis of PEDOT:PSS, polyacrylamide (PAM) and PAM/PEDOT:PSS. (a-c) Nyquist plots of **(a)** dried PEDOT:PSS film, **(b)** PEDOT:PSS on PAM hydrogel and **(c)** pristine PAM hydrogel electrolyte. **(d-e)** Corresponding Bode plots of **(d)** PEDOT:PSS dried film, **(e)** PEDOT:PSS on PAM hydrogel, and **(f)** pristine PAM hydrogel. All measurements were conducted using a stainless-steel coin cell in a two-electrode configuration.

PEDOT:PSS is widely recognized as an organic mixed ionic–electronic conductor (OMIEC) capable of supporting both electronic and ionic transport[36-39]. However, the dried PEDOT:PSS film exhibits a relatively low ionic conductivity ($1.87 \times 10^{-3} \pm 8.36 \times 10^{-4}$ mS/cm), which we attribute to strong electrostatic binding of PSS^- anions to $PEDOT^+$ chains, as well as the presence of residual Na^+ cations. These factors reduce the availability of mobile ions, thereby limiting ion transport. In contrast, the PAM/LiCl hydrogel alone shows a high ionic conductivity of 63.6±15 mS/cm. When PEDOT:PSS is coated on top of the hydrogel, the resulting PEDOT:PSS/PAM hybrid structure retains a comparable ionic conductivity (71.9 ± 19.9 mS/cm), similar in magnitude to the pristine PAM hydrogel. The enhancement arises because moisture from the underlying PAM keeps the PEDOT:PSS hydrated, facilitating ion migration. These results indicate that, in our configuration, the hydrogel effectively supplies mobile ions to the PEDOT:PSS layer, maintaining high ionic conductivity and ensuring that ion transport is not limited by the PEDOT:PSS film.

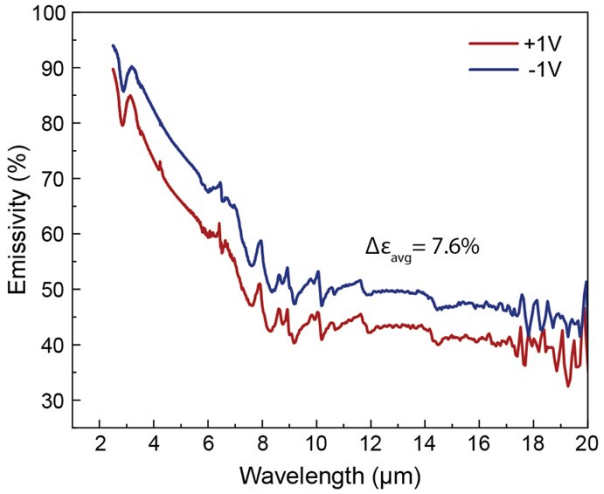

Fig. S6. Emissivity spectra of the planar ASPIRE device on a glass substrate at room temperature, measured in the high-emissivity state (-1 V) and low-emissivity state (+1 V). The weight-averaged emissivity (ε_{avg}) was calculated based on blackbody radiation at human body temperature (34 ℃).

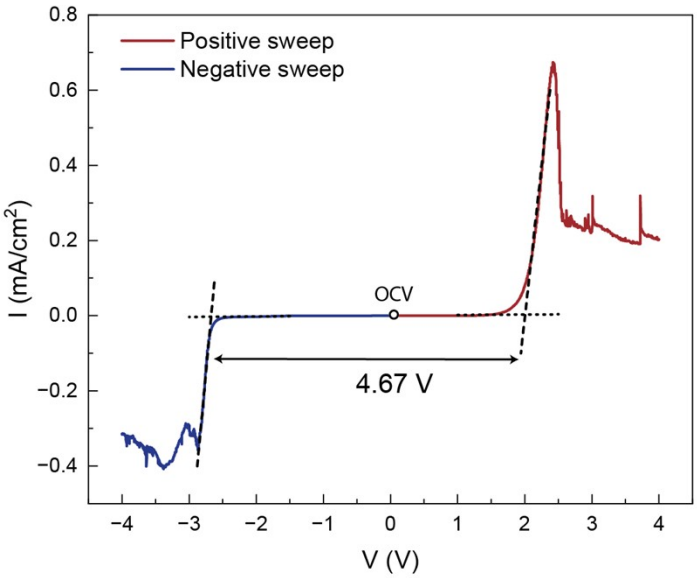

Fig. S7. Linear sweep voltammetry (LSV) stability test of the "water-in-salt" PAM/LiCl hydrogel electrolyte. The measurement was conducted in a stainless-steel coin cell (two-electrode configuration) with a scan rate of 20 mV s^{-1}, over a potential range of –4 V to +4 V. The onset potentials were determined from the intersections of the baseline with the linear fits for both the positive and negative sweeps. No clear signatures of hydrogen evolution reaction (HER) or oxygen evolution reaction (OER) were observed.

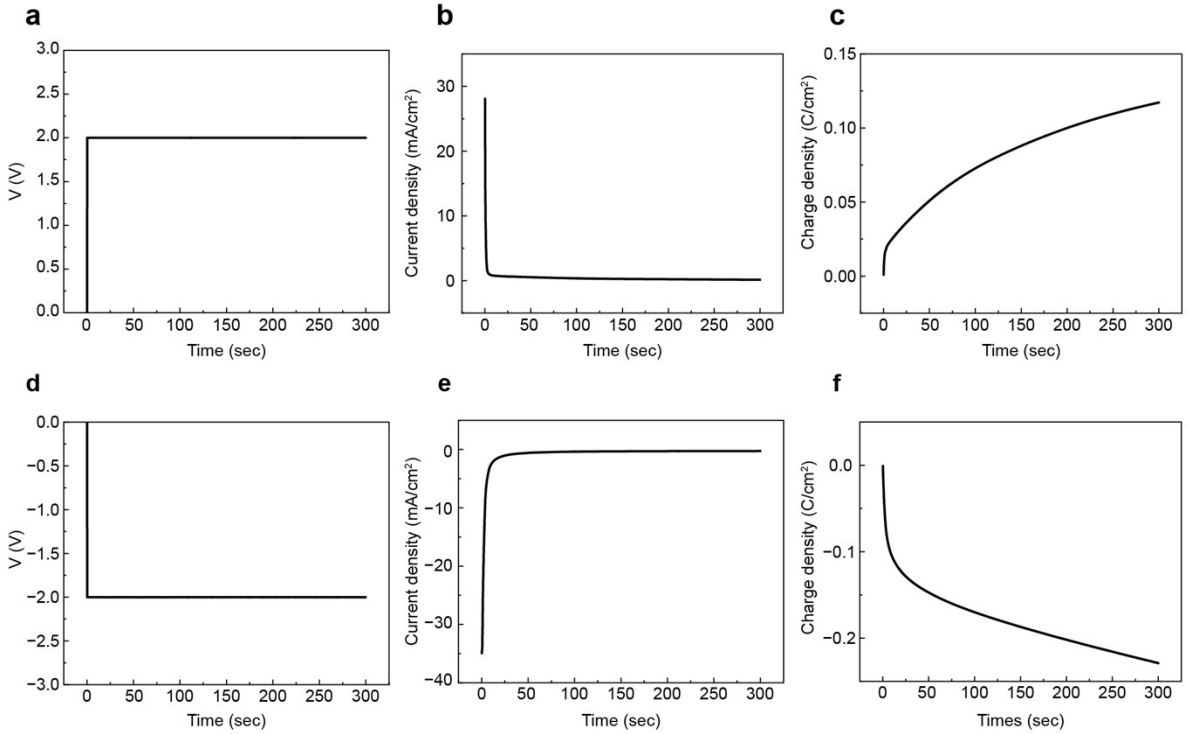

Fig. S8. Chronoamperometry (CA) analysis of the ASPIRE device on a glass substrate. (A) Voltage, **(B)** current, and **(C)** charge of the working electrode as a function of time during the oxidation process. **(D)** Voltage, **(E)** current, and **(F)** charge during the reduction process. The data demonstrate that the ASPIRE device exhibits smooth and stable electrochemical reactions during oxidation and reduction.

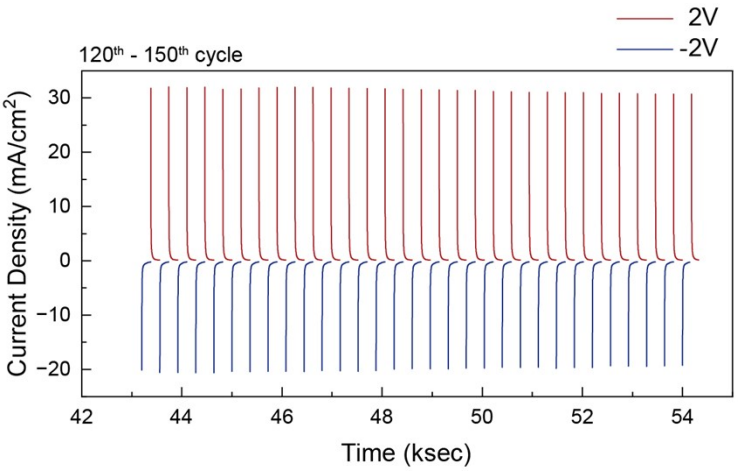

Fig. S9. Continuous chronoamperometry cycling stability of the flat ASPIRE device
The device was subjected to continuous potential stepping between -2 V (reduction, blue) and +2V (oxidation, red). The plot displays a representative segment from the 120th to 150th cycle (approximately 43-54 ksec), derived from the long-term cycling test (Fig 3c). Each cycle consists of a 3-minute oxidation step and a 3-minute reduction step (total 6 minutes per cycle). The highly consistent current density peaks demonstrate robust electrochemical reversibility and structural stability without degradation over extended operation.

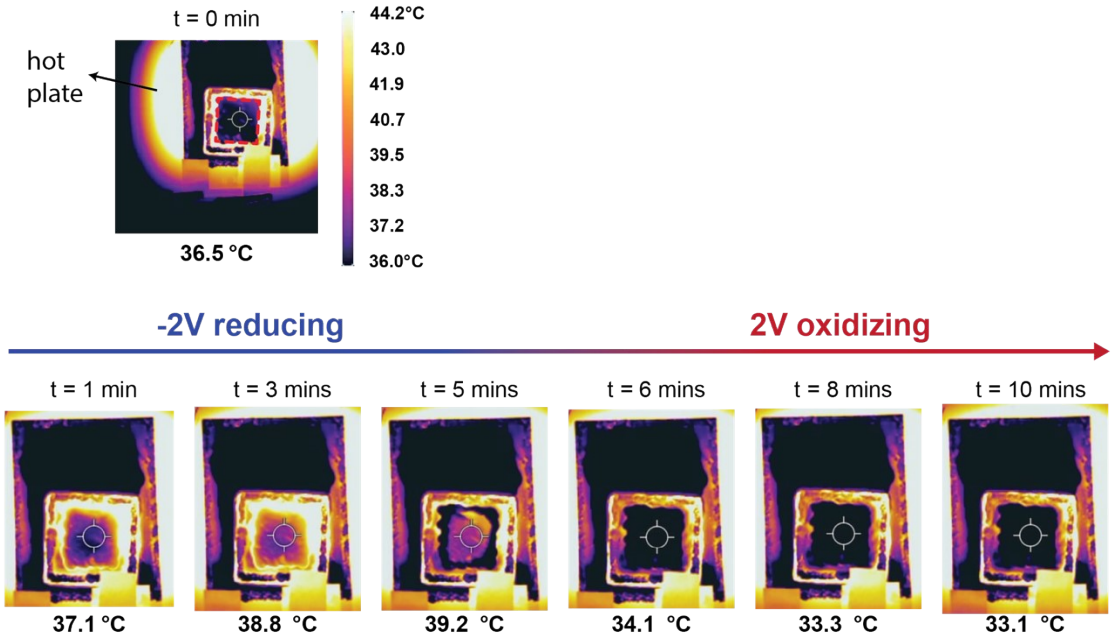

Fig. S10. IR camera images of the ASPIRE on a glass substrate. A constant potential of 2 V (for the low-ε/doped state) and -2 V (for the high-ε/dedoped state) was applied for 5 minutes each, totaling 10 minutes per cycle to ensure complete reduction or oxidation of the top layer of PEDOT:PSS. The change in emissivity of PEDOT:PSS starts from the edge of the device due to a lower ohmic drop near the silver paste around the perimeter. The maximum apparent temperature difference is $\Delta T_{max} = 39.2 - 33.1 = 6.1$℃. The entire electrochromic process can be found in Supplementary Movie 1. The device was tested on a hotplate with a background temperature of 50 ℃.

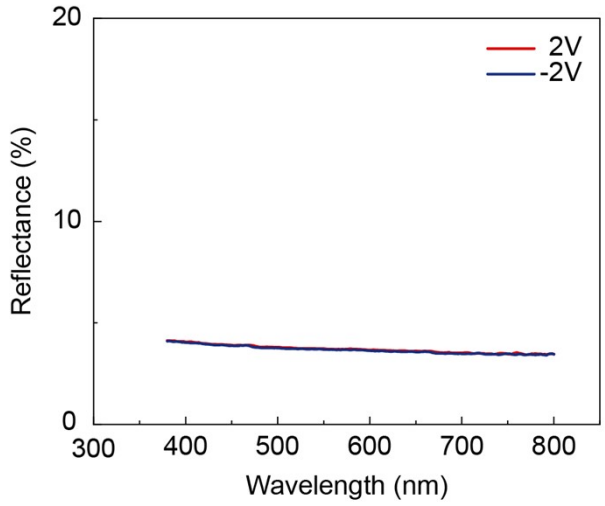

Fig. S11. UV–VIS Spectra of the flat ASPIRE device under different bias states. The visible spectra remain essentially unchanged because the strong broadband absorption of the CNT network dominates the optical responses, masking the subtle color changes of PEDOT:PSS.

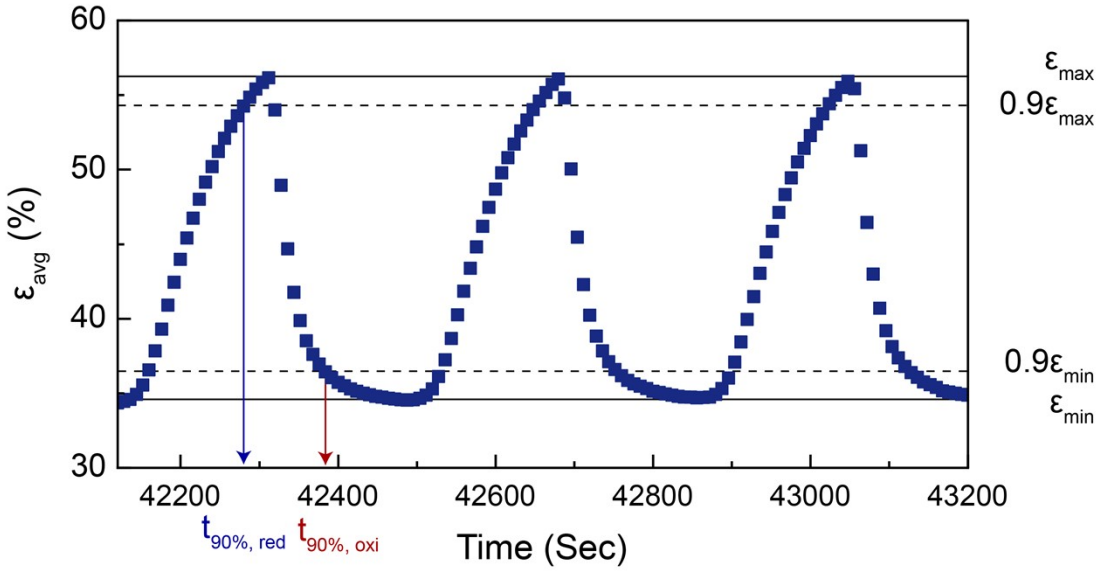

Fig. S12. Switching speed analysis of the flat ASPIRE device, based on the in-situ FTIR time series data from Figure 3C-i.

Four characteristic times were defined:

- $t_{90\%,red}$: the time required for the device to switch from its lowest emissivity (ε_{min}) to 90% of its maximum emissivity (ε_{max}) under a reducing potential,
- $t_{90\%,oxi}$: the time required to switch from ε_{max} to 90% of ε_{min} under an oxidizing potential.
- $t_{start,red}$ and $t_{start,oxi}$: the times when -2 V and +2 V were applied, respectively.

From the definitions, the extracted response times are :

- $\Delta t_{red} = t_{90\%,red} - t_{start,red} = 161$ s
- $\Delta t_{oxi} = t_{90\%,oxi} - t_{start,oxi} = 57$ s

These values indicate that oxidation is significantly faster than reduction, consistent with the intrinsic asymmetry of PEDOT:PSS electrochemical kinetics reported in previous studies[38,40,41]. The slower dedoping (reduction) process has been attributed to the higher activation barrier associated with extracting ions and carriers, in contrast to the faster doping (oxidation) process.

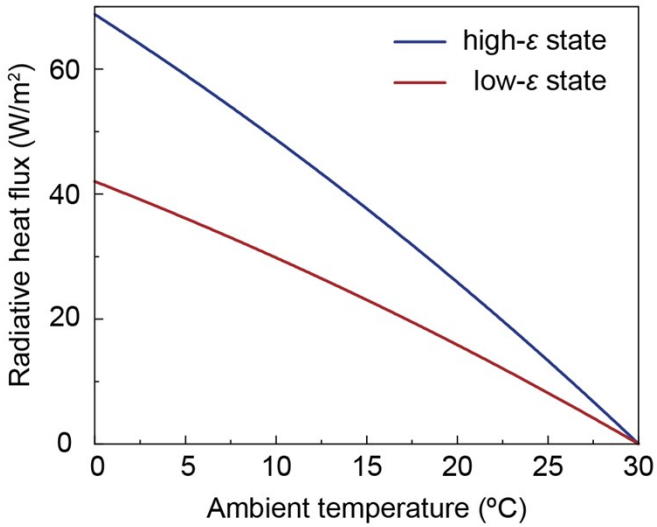

Fig. S13. The calculated radiative heat flux of the planar ASPIRE device. The device temperature is maintained at 30 ℃, while the ambient temperature ranges from 30 ℃ to 0 ℃. The emissivity data of the high-ε/low-ε states are from Fig. 3a.

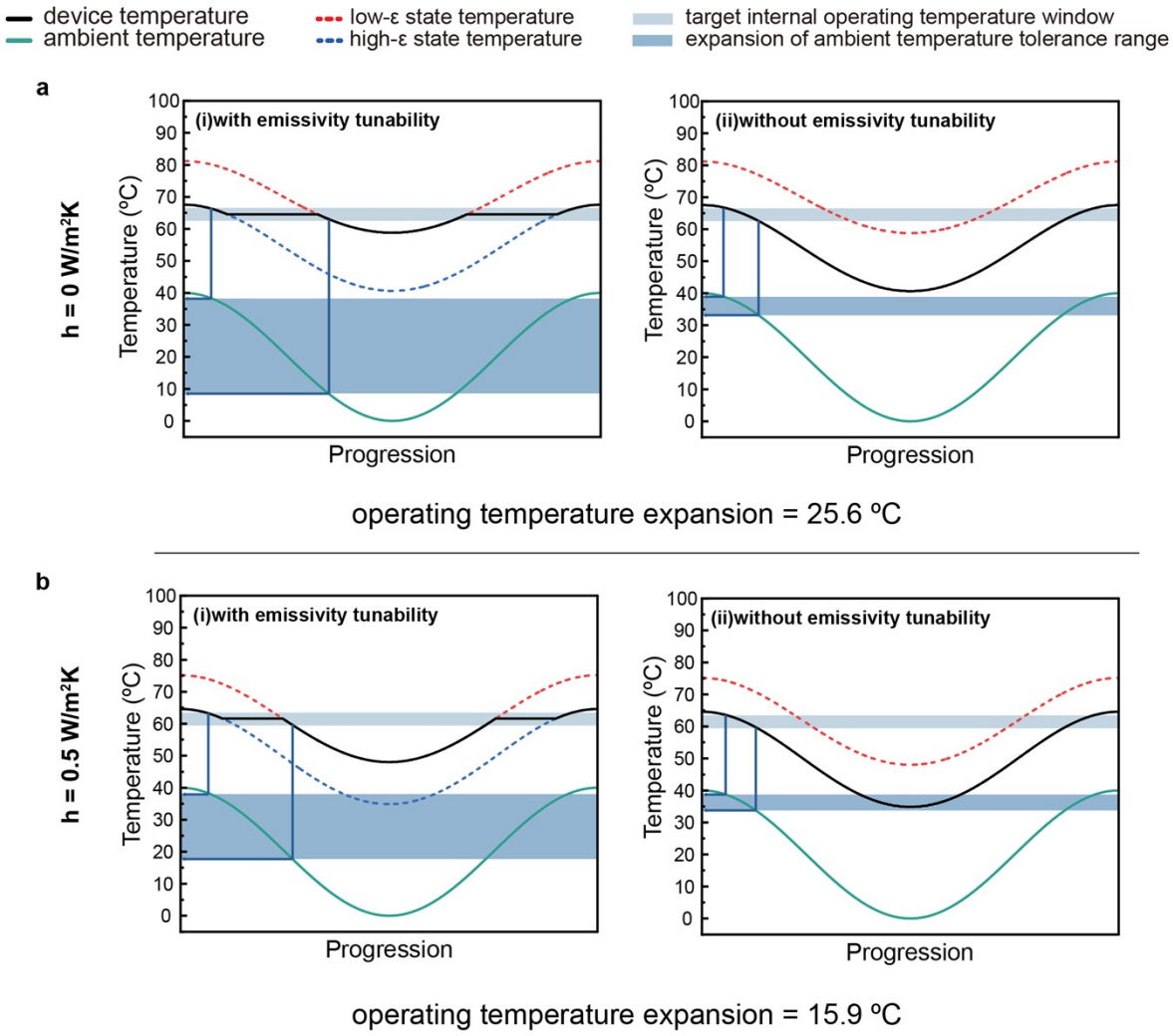

Fig. S14. Operating temperature expansion simulation under extreme convection coefficients. (a) $h = 0 \frac{W}{m^2K}$, and **(b)** $h = 0.5 \frac{W}{m^2K}$. Under these conditions, where radiative heat transfer dominates, the ASPIRE device demonstrates a strong capability for temperature stabilization against ambient fluctuations.

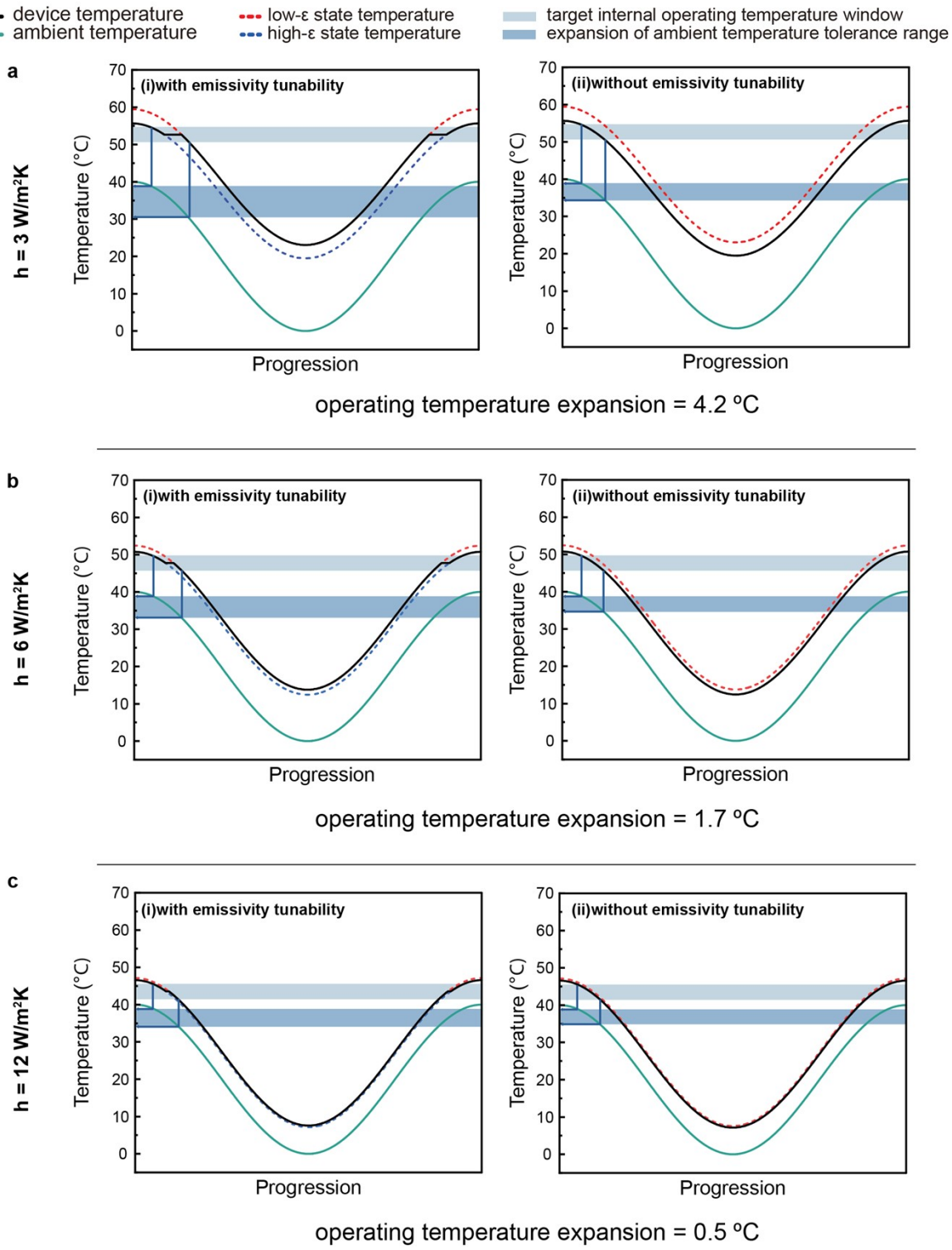

Fig. S15. Operating temperature expansion simulation under moderate to higher coefficients. (a) $h = 3\frac{W}{m^2K}$, (b) $h = 6\frac{W}{m^2K}$, and (c) $h = 12\frac{W}{m^2K}$. Although the ASPIRE device continues to stabilize temperature, its impact becomes less pronounced as convection increases in typical or forced convection environments.

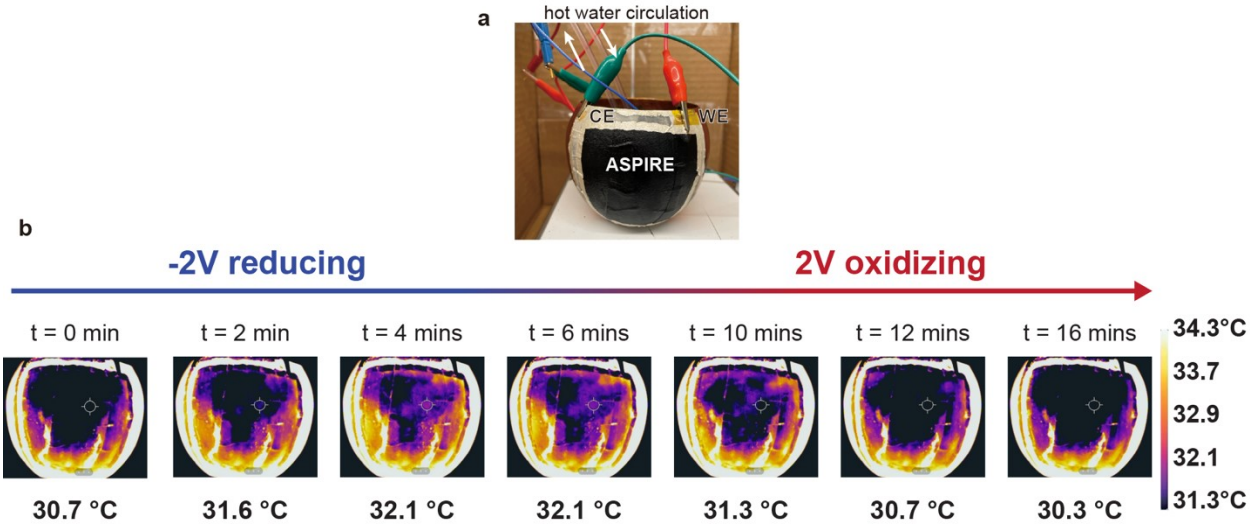

Fig. S16. Thermal regulation performance of the ASPIRE device on a complex-shaped copper cup. (a) Photo of the copper cup ASPIRE device and the experimental setup. WE: working electrode. CE: counter electrode. **(b)** Time-lapse infrared thermal images of the device. The maximum apparent temperature modulation ($^{\Delta T_{max}}$) is calculated as $\Delta T_{max} = T_{6\,min} - T_{16\,min} = 32.1 - 30.3 = 1.8$ °C, achieved by varying the emissivity. Here, t = 6 min corresponds to the reduced (high-ε) state, whereas t = 16 min corresponds to the oxidized (low-ε) state under the applied bias protocol. The actual background temperature of the cup was maintained at 38 ± 0.2 °C.

Table S7. Performance comparison of ASPIRE devices on flat and curved substrates.

Substrate Geometry	Curvature type	Background Temperature (T_{bg})	Apparent Temperature Modulation (ΔT_{max})	Observation of Uniformity
Planar glass	Zero Curvature (K = 0)	50 °C	6.1 °C	Highly uniform
Semi-sphere	Positive Gaussian (K > 0)	38 °C	2.3 °C	Uniform
Copper Cup	Complex/Bulbous (K ≠ 0)	38 °C	1.8 °C	Uniform

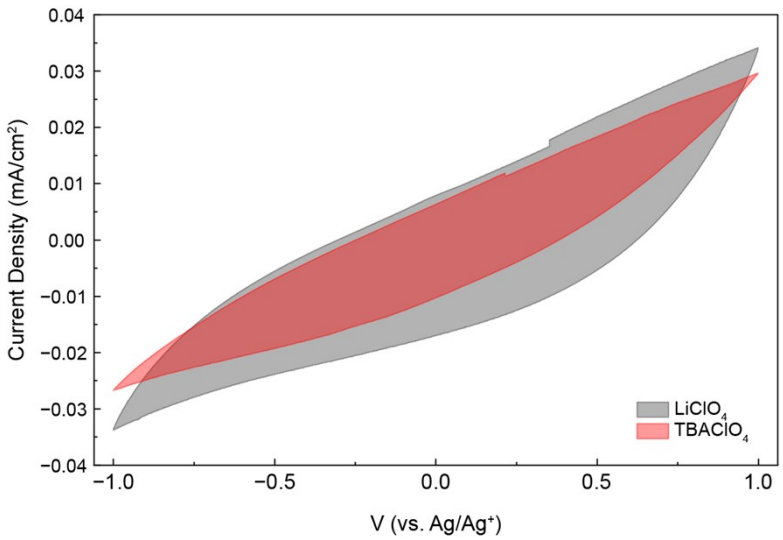

Fig. S17. Comparison of steric hindrance effects on electrochemical performance. Cyclic voltammetry curves of pristine PEDOT:PSS measured in acetonitrile electrolytes containing 0.1 M small cations (Li^+, LiClO4, grey filled area) versus bulky cations (TBA^+, $TBAClO_4$, red filled area). The Li^+ system displays a significantly larger integrated loop area, demonstrating superior charge storage capacity and efficient ion transport. In contrast, the TBA^+ system exhibits a compressed response due to steric hindrance, confirming that bulky ions limit the doping efficiency. Scan rate: 20 mV/s.

Reference

1 Lynch, P. J. *et al.* Mid-Infrared Electrochromics Enabled by Intraband Modulation in Carbon Nanotube Networks. *ACS Applied Materials & Interfaces* **15**, 11225-11233 (2023).

2 Sun, Y. *et al.* Large-Scale Multifunctional Carbon Nanotube Thin Film as Effective Mid-Infrared Radiation Modulator with Long-Term Stability. *Advanced Optical Materials* **9**, 2001216 (2021).

3 Rao, Y. *et al.* Ultra-Wideband Transparent Conductive Electrode for Electrochromic Synergistic Solar and Radiative Heat Management. *ACS Energy Letters* **6**, 3906-3915 (2021).

4 Sui, C. *et al.* Dynamic electrochromism for all-season radiative thermoregulation. *Nature Sustainability* **6**, 428-437 (2023).

5 Zhang, L. *et al.* Further understanding of the mechanisms of electrochromic devices with variable infrared emissivity based on polyaniline conducting polymers. *Journal of Materials Chemistry C* **7**, 9878-9891 (2019).

6 Chen, T.-H. *et al.* A kirigami-enabled electrochromic wearable variable-emittance device for energy-efficient adaptive personal thermoregulation. *PNAS Nexus* **2**, pgad165 (2023).

7 Brooke, R. *et al.* Infrared electrochromic conducting polymer devices. *Journal of Materials Chemistry C* **5**, 5824-5830 (2017).

8 Zhang, X. *et al.* Preparation and performances of all-solid-state variable infrared emittance devices based on amorphous and crystalline WO3 electrochromic thin films. *Solar Energy Materials and Solar Cells* **200**, 109916 (2019).

9 Garcia, G. *et al.* Dynamically Modulating the Surface Plasmon Resonance of Doped Semiconductor Nanocrystals. *Nano Letters* **11**, 4415-4420 (2011).

10 Garcia, G. *et al.* Near-Infrared Spectrally Selective Plasmonic Electrochromic Thin Films. *Advanced Optical Materials* **1**, 215-220 (2013).

11 Cirpan, A., Argun, A. A., Grenier, C. R. G., Reeves, B. D. & Reynolds, J. R. Electrochromic devices based on soluble and processable dioxythiophene polymers. *Journal of Materials Chemistry* **13**, 2422-2428 (2003).

12 Zhao, Y. *et al.* Preparation of WO3 Films with Controllable Crystallinity for Improved Near-Infrared Electrochromic Performances. *ACS Sustainable Chemistry & Engineering* **8**, 11658-11666 (2020).

13 Yen, H.-J. & Liou, G.-S. Solution-Processable Novel Near-Infrared Electrochromic Aromatic Polyamides Based on Electroactive Tetraphenyl-p-Phenylenediamine Moieties. *Chemistry of Materials* **21**, 4062-4070 (2009).

14 Singh, R., Tharion, J., Murugan, S. & Kumar, A. ITO-Free Solution-Processed Flexible Electrochromic Devices Based on PEDOT:PSS as Transparent Conducting Electrode. *ACS Applied Materials & Interfaces* **9**, 19427-19435 (2017).

15 Cai, G. *et al.* Highly Stable Transparent Conductive Silver Grid/PEDOT:PSS Electrodes for Integrated Bifunctional Flexible Electrochromic Supercapacitors. *Advanced Energy Materials* **6**, 1501882 (2016).

16 Kai, H., Suda, W., Ogawa, Y., Nagamine, K. & Nishizawa, M. Intrinsically Stretchable Electrochromic Display by a Composite Film of Poly(3,4-ethylenedioxythiophene) and Polyurethane. *ACS Appl Mater Interfaces* **9**, 19513-19518 (2017).

17 Yan, C. *et al.* Stretchable and Wearable Electrochromic Devices. *ACS Nano* **8**, 316-322 (2014).

18 Pagès, H., Topart, P. & Lemordant, D. Wide band electrochromic displays based on thin conducting polymer films. *Electrochimica Acta* **46**, 2137-2143 (2001).
19 Winslow, C.-E., Gagge, A. & Herrington, L. The influence of air movement upon heat losses from the clothed human body. *American Journal of Physiology-Legacy Content* **127**, 505-518 (1939).
20 Amb, C. M., Dyer, A. L. & Reynolds, J. R. Navigating the Color Palette of Solution-Processable Electrochromic Polymers. *Chemistry of Materials* **23**, 397-415 (2010).
21 Reynolds, J. R., Thompson, B. C. & Skotheim, T. A. *Conjugated Polymers: Properties, Processing, and Applications*. 4 edn, (CRC Press, 2019).
22 A.j. Heeger, N. S. S., E.B. Namdas. *Semiconducting and Metallic Polymers*. (Oxford Graduate Texts, 2010).
23 Lee, K., Heeger, A. J. & Cao, Y. Reflectance of polyaniline protonated with camphor sulfonic acid: Disordered metal on the metal-insulator boundary. *Phys Rev B Condens Matter* **48**, 14884-14891 (1993).
24 Lee, K., Menon, R., Yoon, C. O. & Heeger, A. J. Reflectance of conducting polypyrrole: Observation of the metal-insulator transition driven by disorder. *Phys Rev B Condens Matter* **52**, 4779-4787 (1995).
25 Fox, M. *Optical properties of solids*. 2 edn, (Oxford University Press Oxford, 2010).
26 Gu, S. *et al.* Effects of Ion Valence States and Radii on the Performance of Solid-State PEDOT:PSS Electrochromic Devices. *ACS Applied Materials & Interfaces* **16**, 63978-63988 (2024).
27 Lyu, D. *et al.* Operando NMR electrochemical gating studies of ion dynamics in PEDOT:PSS. *Nat Mater* **22**, 746-753 (2023).
28 Liu, W. *et al.* Scalable and High-Performance Infrared Electrochromic Devices Enabled by Solvent-Engineered PEDOT/PSS Films. *ACS Applied Materials & Interfaces* **17**, 37175-37184 (2025).
29 Suo, L. *et al.* "Water-in-salt" electrolyte enables high-voltage aqueous lithium-ion chemistries. *Science* **350**, 938-943 (2015).
30 Zhigalenok, Y. *et al.* Water activity: the key to unlocking high-voltage aqueous electrolytes? *Journal of Materials Chemistry A* **12**, 33855-33869 (2024).
31 Zhang, J. *et al.* “Water-in-salt” polymer electrolyte for Li-ion batteries. *Energy & Environmental Science* **13**, 2878-2887 (2020).
32 Tamai, Y., Tanaka, H. & Nakanishi, K. Molecular Dynamics Study of Polymer−Water Interaction in Hydrogels. 2. Hydrogen-Bond Dynamics. *Macromolecules* **29**, 6761-6769 (1996).
33 Tamai, Y., Tanaka, H. & Nakanishi, K. Molecular Dynamics Study of Polymer−Water Interaction in Hydrogels. 1. Hydrogen-Bond Structure. *Macromolecules* **29**, 6750-6760 (1996).
34 Ji, D. & Kim, J. Trend of Developing Aqueous Liquid and Gel Electrolytes for Sustainable, Safe, and High-Performance Li-Ion Batteries. *Nano-Micro Letters* **16**, 2 (2023).
35 de Dear, R. J., Arens, E., Hui, Z. & Oguro, M. Convective and radiative heat transfer coefficients for individual human body segments. *Int J Biometeorol* **40**, 141-156 (1997).
36 Inal, S., Malliaras, G. G. & Rivnay, J. Optical study of electrochromic moving fronts for the investigation of ion transport in conducting polymers. *Journal of Materials Chemistry C* **4**, 3942-3947 (2016).

37 Paulsen, B. D., Tybrandt, K., Stavrinidou, E. & Rivnay, J. Organic mixed ionic-electronic conductors. *Nat Mater* **19**, 13-26 (2020).
38 Keene, S. T., Rao, A. & Malliaras, G. G. The relationship between ionic-electronic coupling and transport in organic mixed conductors. *Sci Adv* **9**, eadi3536 (2023).
39 Tan, S. T. M. *et al.* Mixed Ionic–Electronic Conduction, a Multifunctional Property in Organic Conductors. *Advanced Materials* **34**, 2110406 (2022).
40 Wu, R., Paulsen, B. D., Ma, Q. & Rivnay, J. Mass and Charge Transport Kinetics in an Organic Mixed Ionic–Electronic Conductor. *Chemistry of Materials* **34**, 9699-9710 (2022).
41 Rebetez, G., Bardagot, O., Affolter, J., Réhault, J. & Banerji, N. What Drives the Kinetics and Doping Level in the Electrochemical Reactions of PEDOT:PSS? *Advanced Functional Materials* **32** (2021).